Fuel 305 (2021) 121606

Contents lists available at ScienceDirect

Fuel

journal homepage: www.elsevier.com/locate/fuel

Full Length Article

Monitoring oil displacement and CO_2 trapping in low-permeability media using NMR: A comparison of miscible and immiscible flooding

Mingyu Cai [a,b], Yuliang Su [a,b,*], Yongmao Hao [a,b], Yingchun Guo [d], Derek Elsworth [c], Lei Li [a,b], Dongsheng Li [a,b], Xinyu Li [a,b]

[a] Key Laboratory of Unconventional Oil & Gas Development, Ministry of Education, Qingdao 266580, China
[b] School of Petroleum Engineering, China University of Petroleum (East China), Changjiang West Road 66, Economic Technical Development Zone, Qingdao, Shandong Province 266580, PR China
[c] Energy and Mineral Engineering & Geosciences, The Pennsylvania State University, 110 Hosler Building, University Park, PA 16802, United States
[d] Research Institute of Petroleum Exploration and Development, SINOPEC Shengli Oilfield, Jinan Road 258, Dongying District, Dongying, Shandong Province 266580, PR China

ARTICLE INFO

Keywords:
Immiscible/miscible displacement
Nuclear magnetic resonance
Enhanced oil recovery
CO_2 trapping
Low-permeability formation

ABSTRACT

Dynamic monitoring of the internal fluid distribution during CO_2 immiscible/miscible flooding provides a crucial window for illuminating key processes controlling displacement and transport. We used online low-field nuclear magnetic resonance (NMR) imaging to monitor CO_2 flooding under different reservoir pressures in low-permeability siltstone core plugs pre-saturated with stock tank oil from the Chang7_2 Formation in China. Immiscible and miscible styles of fluid displacement were triggered by flooding at pressures of 8 and 16 MPa, respectively. To visualize the oil distribution, NMR T_2 and T_1–T_2 spectra and one-dimensional frequency (1D-FQ), and magnetic resonance imaging (MRI) were conducted to obtain the overall and spatially distributed saturations. The results show that recovery by miscible flooding (69.4%) was twice more than that by immiscible flooding (32.6%). The effect of the extraction of lighter components on oil viscosity and density after CO_2 injection was negligible compared to the changes in miscibility. CO_2 concentrations at the leading edge of the miscible zone (0.526) were higher than in the immediately adjacent transition zone (0.1); the dimensionless widths were 0.76 and 0.44, respectively. The CO_2 retention rate following miscible flooding was 10.59% higher than that due to immiscible flooding, primarily due to remnant dissolved CO_2 in the oil. In contrast, immiscible flooding limited the solubility of CO_2 and led to solubility and residual trapping. These observations have a significant impact on defining oil and CO_2 budgets, modes of transport, and storage for enhanced oil recovery and CO_2 sequestration.

1. Introduction

The use of traditional water flooding to improve enhanced oil recovery (EOR) is problematic in unconventional low-permeability reservoirs [1–3] due to 1) high injection pressure that makes establishing an effective pressure system difficult, 2) slow pressure propagation rates and near-wellbore water accumulation that rapidly decrease production, and 3) the propensity for capillary and miscibility-driven fingering and premature water breakthrough. Laboratory and field observations confirm that CO_2 is a potential displacement agent for unconventional reservoirs [4–7]. Injected CO_2 diffuses into the matrix through both natural and hydraulic fracturing, increasing the formation pressure and volume expansion and decreasing the crude oil viscosity [8]. The miscibility of CO_2 with oil simultaneously reduces the interfacial tension and increases mobility [9,10]. The success of various EOR mechanisms largely depends on reservoir conditions (temperature, pressure, rock wettability, permeability, and porosity) [11–13], and reservoir rock and fluid composition [14,15]. Multiphase reservoir simulators conduct CO_2–water–oil flow and reactive transport through large-scale computing. The impact of reservoir permeability, porosity, formation thickness and depth on CO_2 injection/storage and enhanced oil recovery can be systematically analyzed with geological and statistical models. Such integrated simulations provide useful insights into CO_2 sequestration and commercial oil and gas recovery [16]. Understanding and

* Corresponding author.
E-mail address: suyuliang@upc.edu.cn (Y. Su).

https://doi.org/10.1016/j.fuel.2021.121606
Received 23 April 2021; Received in revised form 10 July 2021; Accepted 28 July 2021
Available online 7 August 2021

quantifying the respective roles and relative dominance among the various EOR mechanisms is key to optimizing performance – but requires detailed observation of dynamic processes that are intrinsically challenging to conduct even in the laboratory [17–19].

Thus, acquiring spatially resolved time-series information on fluid distributions through core floods is of interest [20]. However, dynamic spatially resolved monitoring of core floods has traditionally not been possible. Therefore, such systems are treated as black box models where only the volumes and compositions of recovered fluids are measured [21–23], and the internal behavior is merely conjectured. Numerous techniques used to inform laboratory core floods include surface-characterization techniques at the millimeter-nanometer scale, such as atomic force microscopy (AFM) [24,25] and scanning electron microscopy (SEM) [9,26] and imaging techniques capable of revealing spatial heterogeneities in saturation at the pore-to-core scale (X-ray CT [27–29] and nuclear magnetic resonance (NMR) imaging [30–32]). NMR imaging measures the nuclear spin density and relaxation time (longitudinal and transverse) that may be linked to the fluid flow velocity and the self-diffusion coefficient. Such measurements are rapid, non-invasive, and spatially resolved; thus, NMR is one of the most useful tools for studying pore structure and its internal fluid flow [33–36].

In this study, we propose analytical methods to quantitatively analyze multi-component mobility, the displacement of the (im)miscibility front, the evolution of the transition/miscible zone, along with CO_2 retention and trapping mechanisms. Online nuclear magnetic resonance spectroscopy (online NMR) is used to monitor CO_2 flooding in immiscible and miscible states. The overall oil recovery was calculated based on the NMR T_2 spectra. The distribution of residual oil was observed on cross-sectional magnetic resonance images (MRI), and a more detailed distribution of different components was analyzed by T_1–T_2 spectra. The evolution of the CO_2 oil interfaces during miscible and immiscible flooding was clarified by one-dimensional frequency (1D-FQ) synthesis based on the spin-echo single-point imaging technique and mass balance by constraining the spatial and dynamic distribution of fluid saturation throughout the core. The amount of CO_2 dissolution and capillary trapping was distinguished through phase equilibrium calculations combined with the measurement of the mass balance of oil/gas at the outlet.

2. Experimental section

2.1. Materials

Stock tank oil from the Chang7_2 Formation in the Changqing oil field was used to saturate the cores. The oil density ranged from 0.835 to 0.845 g/cm^3, and the oil viscosity ranged from 2.46 to 2.65 mPa·s as pressure increases from 8 to 16 MPa at a temperature of 313 K. Table 1 presents detailed parameters defining the oil. The composition of the oil sample was analyzed using an Agilent 7890A chromatograph. The component properties (including the mole fraction, m; the critical pressure and temperature, P_c and T_c, respectively; the acentric factor, a_c; and the mole weight, M_w) were corrected by fitting the constant composition expansion (CCE) test results. To ensure clarity in the scanned images, the saturated cores were pre-screened with MRI to preferentially select the cores with low porosity and permeability and high pore-throat connectivity. Table 2 lists the dimensions and helium-measured porosities of the core samples (e.g., dry weight, W_{dry}; length, L; diameter, d; porosity, ϕ; and Klinkenberg-corrected permeability, k_∞). Two low-permeability siltstone core samples with similar basic parameters were used to conduct CO_2 flooding in an immiscible and miscible state. The core lengths were ~60 mm, the diameters were 2.53 mm, and the porosity and permeability were ~17% and 8.2 mD, respectively.

Table 1
The mole percent and properties of different components in Chang7_2 stock tank oil.

Component	m/%	P_c/MPa	T_c/K	a_c	M_w
CH_4	0.18	4.60	190.60	0.01	16.04
C_2H_6	0.21	4.88	305.40	0.10	30.07
C_3H_8	1.60	4.25	369.80	0.15	44.10
IC_4	0.74	3.65	408.10	0.18	58.12
NC_4	1.70	3.80	425.20	0.19	58.12
IC_5	2.71	3.38	460.40	0.23	72.15
NC_5	3.37	3.37	469.60	0.25	72.15
FC_6	8.27	3.29	507.50	0.28	86.00
FC_7	4.92	3.14	543.20	0.31	96.00
FC_8	5.58	2.95	570.50	0.35	107.00
FC_9	4.90	2.73	598.50	0.39	121.00
FC_{10}	4.06	2.53	622.10	0.44	134.00
$C_{11}+$	61.75	1.65	998.86	0.62	223.59

2.2. Apparatus

Fig. 1 shows a schematic of the assembled core flooding systems used in the experiments. The experimental scheme primarily comprises of 1) an injection system that provides heated CO_2 at a fixed pressure or rate; 2) a core holder system that heats and pressurizes the fixed core through fluorocarbon oil circulation; 3) an outlet control system that includes a back-pressure-regulator and a collection device; and 4) a data acquisition unit for NMR data acquisition and inversion. A MacroMR12-150H-I NMR core analysis system was employed to measure the proton magnetic resonance (PMR) of oil in the core plugs. The permanent magnet of the NMR spectrometer was 0.3 ± 0.05 T, with a resonant frequency of 12.797 MHz. The probe coil diameter was 25 mm and the temperature of the magnet was 305.00 ± 0.02 K. The echo and recovery times were 1500 and 0.1 ms, respectively; the echo and scanning numbers were 4000 and 32, respectively.

T_1 and T_2 relaxation in heavy oils describes the overlapping relaxation distributions of all the molecular components within the fluid [37]. Transverse T_2 relaxation describes the decay of coherence among nuclear spins in the x-y plane as a result of time-varying magnetic fields, whereas longitudinal T_1 relaxation describes the energy exchange process of returning to thermal equilibrium along the z-axis of the static applied field [38,39]. The measurement data can be expressed as [40]:

$$\mathrm{M}(\tau_1,\tau_2)=\iint\left(1-2e^{-\tau_1/T_1}\right)e^{-\tau_2/T_2}\mathrm{F}(T_1,T_2)dT_1dT_2+E(\tau_1,\tau_2) \quad (1)$$

The NMR relaxation times of the liquid hydrocarbons can be split into different additive rates as [41]:

$$\frac{1}{T_{1,2}}=\frac{1}{T_{1,2}^{\mathrm{intra}}}+\frac{1}{T_{1,2}^{\mathrm{inter}}}+\frac{1}{T_{1,2}^{\mathrm{elec}}} \quad (2)$$

where τ_1 and τ_2 represent the recovery and echo time, respectively; $E(\tau_1,\tau_2)$ are white Gaussian noise; $\mathrm{F}(T_1,T_2)$ are the spectral functions to be solved; $\left(1-2e^{-\tau_1/T_1}\right)e^{-\tau_2/T_2}$ is the integral kernel that relates$T_{1,2}$ and $\tau_{1,2}$; T^{intra} is the intramolecular interaction; T^{inter} is the intermolecular relaxation; and T^{elec} denotes the relaxation related to spin rotation.

The rock sample was composed of pores of different sizes; therefore, the signal strength L of each pixel is the superposition of the relaxation signals of different pores and can be expressed as:

$$L=L_0exp(-T_e/T_2) \quad (3)$$

where L_0 is a constant proportional to the number of hydrogen atoms in the pixel element, and T_e is the echo time. As the hydrocarbon is driven

Table 2
Basic physical parameters of selected low permeability cores.

Core No.	W_{dry}/g	L/mm	d/mm	ϕ/%	k_∞/mD
# 1	53.44	60.6	2.53	17.00	8.17
# 2	53.00	59.6	2.53	17.49	8.35

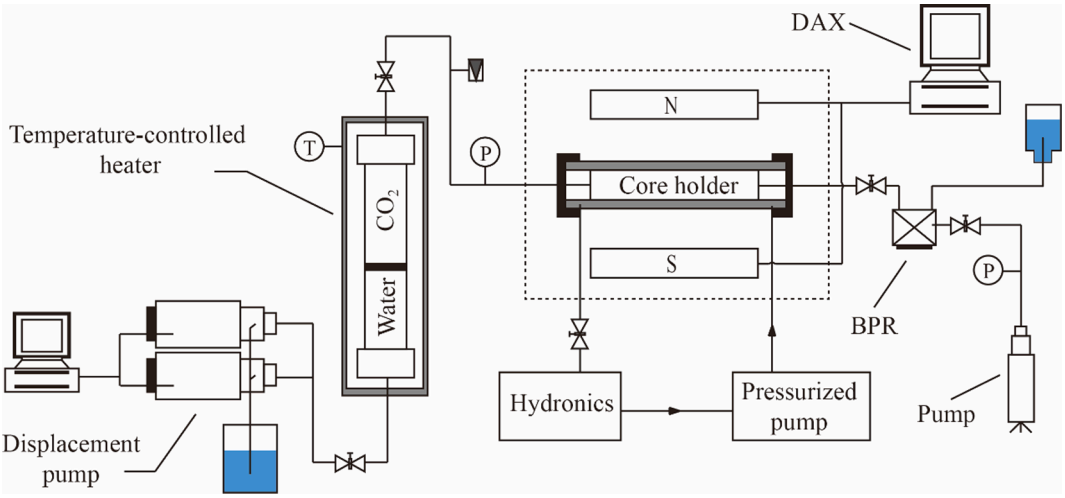

Fig. 1. Schematic diagram of the experimental setup.

out by CO_2, the number of hydrogen atoms in the pores decreases, and the oil saturation at time t in the pore space can be calculated using the following equation:

$$S_o(t) = \frac{\sum L(t)}{\sum L_{int}} S_{oi} \tag{4}$$

where S_{oi} is the initial oil saturation, and $\sum L_{int}$ and $\sum L(t)$ are the total signal intensity of all the pixels in the initial state (without CO_2 injection) and time t.

2.3. Experimental procedures

The temperature of the core flooding system was set to 313 K to represent the in-situ reservoir temperature. The minimum miscibility pressure (MMP) of the dead oil sample was simulated as 12.7 MPa; thus, the immiscible and miscible flooding back-pressures were set at 8 and 16 MPa, respectively. The corresponding confining pressures for immiscible and miscible flooding were set to 10 and 18 MPa, respectively, to maintain a constant effective (skeletal) stress. The room temperature, which impacts the calculation of fluid properties collected at the outlet, was measured as 299.2 K. The experimental procedure consisted of several steps. First, the core samples were placed in an oven at 378 K for 24 h, then removed and air-cooled to room temperature before obtaining the dry weight. The NMR T_2 and T_1–T_2 spectra, volume, and porosity of the cores were measured. Second, the samples were vacuum-desaturated and pressure-saturated with oil at 15 MPa for 12 h. The oil-saturated cores were weighed after aging for 24 h. The NMR T_2 and T_1–T_2 spectra of the saturated cores were measured. Third, the NMR parameters were calibrated to establish a relationship between the average existing oil mass and the NMR signal from the measured porosity and mass of the injected oil. Fourth, the cores were placed into the core holder and heated to 313 K while increasing the confining pressure (to 10 or 18 MPa), and back-pressure (8 or 16 MPa). Fifth, to ensure that the back-pressure pipe was filled with oil and tightly connected to the core holder, oil was injected at a constant upstream pressure till it arrived at the outlet. After the pressure stabilized, T_2 and T_1–T_2 spectra, MRI, and 1D-FQ were recorded as the initial state. Sixth, the CO_2 was heated to 313 K in an intermediate container and pressurized to 8.2 or 16.2 MPa before injecting at a constant rate of 0.01 mL/min. Seventh, the gas and oil produced at the outlet was collected. The T_2 spectrum and the 1D-FQ at injection volumes of 0.1, 0.2, 0.4, 0.6, 0.8, 1.0, 1.2 and 1.5 PV were recorded as the final state; the MRI and T_1–T_2 spectrum at the initial and final states of displacement were measured.

3. Results and discussion

3.1. Enhanced oil recovery for miscible/immiscible flooding

Fig. 2 shows the T_2 distribution for the fully saturated core and the core after the injection of different fractional pore volumes of CO_2. The T_2 distributions for the fully oil-saturated cores are shown as blue lines, which exhibit an evident multimodal distribution. The first dominant peak occurred at ~1–10 ms with fast relaxation, indicating micropore characteristics. The second peak was between 10 ms and 100 ms and corresponded to the macropores in the cores. The third peak had a slow relaxation time of >100 ms, indicating the presence of cracks within the core samples. Fig. 2 shows that the decline in the T_2 amplitude for the miscible flooding was more rapid and dramatic than that for immiscible flooding.

The displacement efficiency of the cores was calculated from the ratio of the total T_2 amplitude at each test point to the fully saturated state. As CO_2 was injected, the displacement efficiency increased faster in the miscible state than in the immiscible state. Fig. 3 shows that the displacement efficiency increased rapidly with the injection volume of CO_2 before reaching an inflection point A (or A'). This inflection point was determined via a slope decline threshold of 40%. More specifically, when the slope of line AB was <40% of the slope of line OB and the slope of subsequent segments had no upward trend, point A was the inflection point of the displacement efficiency curve. For the immiscible state (Fig. 3(a)), the production rate slowed down significantly after a CO_2 injection of 0.6 PV (with a slope declined to ~40% of line OB, and oil recovery was 28%), with an ultimate recovery factor of 32.6%. Comparatively, the miscible displacement efficiency (Fig. 3(b)) increased rapidly before a CO_2 injection of 0.4 PV (with a slope declined to ~21% of line OB). When the injected CO_2 reached 0.4 and 1.5 PV, the recovery factors were 57% and 69.4%, respectively. Because the temperatures were identical in both cases, the enhanced oil recovery was related solely to the pressure and transition in the displacement mechanism from immiscible to miscible flooding.

NMR signals inspecting the hydrocarbon in micropores, macrospores, and cracks were recorded; and the variation of the remaining oil with injected CO_2 volume was evaluated from the calibration (Fig. 4). The displacement efficiency of immiscible flooding (Fig. 4(a)) within large pores increased rapidly in the early stage but decreased in the middle stage before stabilizing at ~38%. The presence of cracks contributed to the majority of the oil recovered when ~0.5 PV of gas was injected and subsequently it retained ~65% of the displacement efficiency. This likely resulted from the early migration of expanding oil from the pores into the cracks, which then acted as a dominant transport

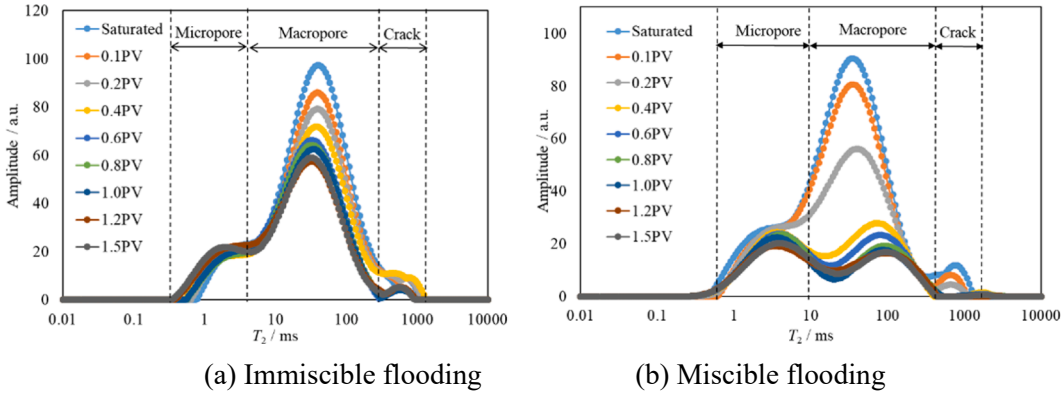

Fig. 2. Changes in NMR T_2 spectrum of oil with injected CO_2 volume for immiscible (a) and miscible (b) states.

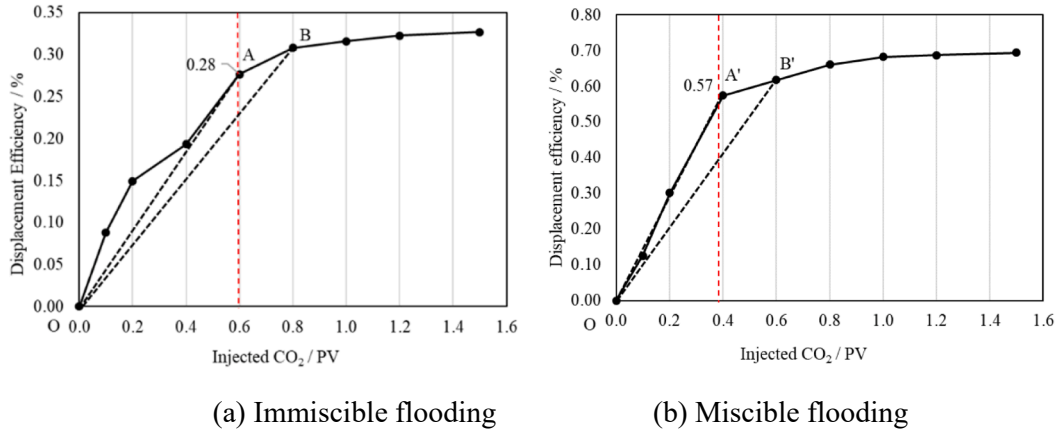

Fig. 3. Changes in displacement efficiency with injected CO_2 volume.

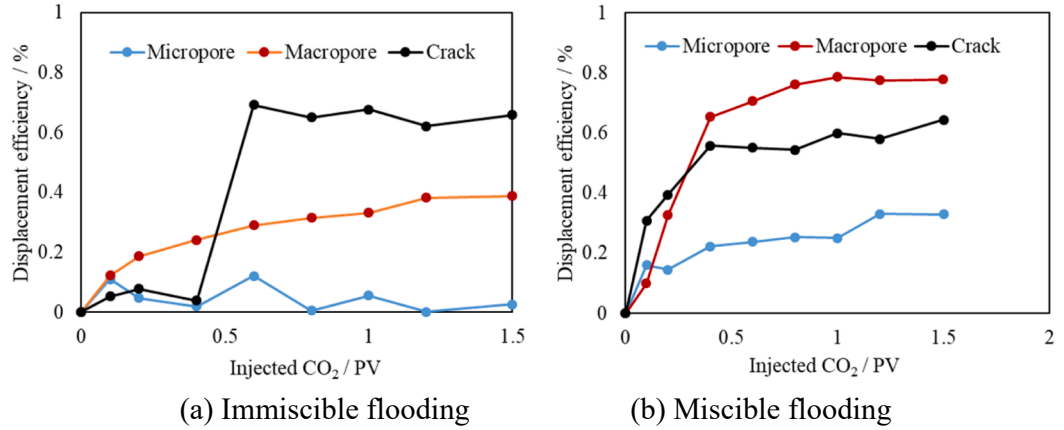

Fig. 4. Displacement efficiency of different pore spaces.

channel. The blue line indicates that a small amount of oil within the micropores was displaced by immiscible flooding. The transition zone mechanism during displacement hindered CO_2 to enter some micropores due to the high capillary force while hydrocarbon components could diffuse into the bulk CO_2 region, reducing the oil in the micro pores. However, the dissolution of CO_2 simultaneously decreases the oil viscosity and oil–gas interfacial tension, allowing oil to enter smaller pores and resulting in displacement efficiency fluctuations of micropores with the injection volume of CO_2.

Miscible flooding had a significant but contrasting impact on the displacement of pores of different sizes. The displacement efficiency for all three pore-size populations initially increased rapidly then decreased after ~0.4 PV of CO_2 injection. After flooding, the oil fractions recovered from micropores, macropores, and cracks were 33%, 78%, and 64%, respectively. The oil remaining in the cracks might be further recovered by continuous CO_2 injection.

3.2. *Residual oil distribution and components extraction*

Figs. 5 and 6 show a series of MRI scans to monitor and compare the

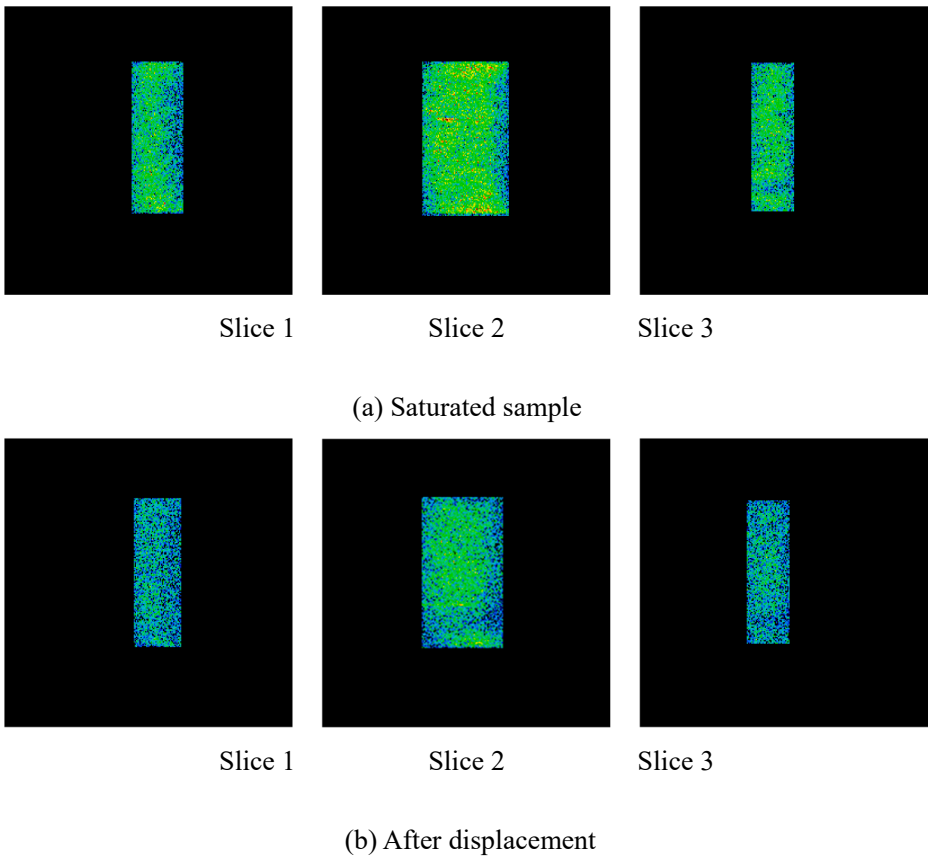

Fig. 5. MRI of oil saturation pre-and post-immiscible flooding.

saturation distributions from immiscible and miscible SC-CO_2 flooding by contrasting the states before and after displacement. The thickness of one target slice in the MRI image was 7 mm, and the interval between slices was 0.5 mm. Three slices were represented as slices 1, 2, and 3, respectively. The images reveal the heterogeneity of the fluid distribution in the core plug. The brighter areas (red and green) indicate higher signal strength and correspond to higher oil saturation, whereas darker areas (blue and black) indicate lower signal strength and correspond to lower oil saturation.

Fig. 5(b) shows that the remaining oil after immiscible flooding was distributed evenly in the flow direction, except for the low signal area adjacent to the core outlet. Thus, despite the low porosity and permeability in the area, the oil can be effectively displaced owing to high connectivity; this is possibly an artifact of the end-core boundary condition. The remaining oil is significantly more reduced after miscible flooding than after immiscible flooding and is mostly concentrated at the outlet (Fig. 6(b)).

For substances in a given magnetic field, T_2 relaxation occurs with T_1 relaxation and additional processes (static local fields and spin "flip-flops") that cause T_2 relaxation without affecting T_1 [42]. Thus, relaxation always occurs at a faster rate for T_2 than for T_1; therefore, the T_1 relaxation time is always greater than or equal to T_2 [43,44]. The T_1 and T_2 relaxation times of substances with lower molecular weights (e.g., water, CO_2, and light hydrocarbon) are longer, whereas the T_2 relaxation times of substances with higher molecular weights (e.g., heavy hydrocarbons and asphaltene solids) are relatively shorter [45–47]. Accordingly, the composition of fluids may be recovered from the spectral peaks in the T_1–T_2 maps [48]. Fig. 8 shows the T_1–T_2 maps of the saturated cores. Because the pore size and initial saturation distributions of the miscible and immiscible displacements were similar, the features of the T_1–T_2 maps are also similar.

Correlations exist between the NMR T_1/T_2 ratio and oil/gas mobility in porous media [39,43,45]. Comparing the T_1–T_2 maps of previous studies with those of this work (Fig. 7) determine the regions mapped for the oil-bearing low-permeability sandstone in this study (Fig. 8). Because of the dipole interaction, the molecular motion of bulk fluids (e.g., oil and water) is relatively balanced, and the T_1/T_2 ratio approaches one. Because the dipole interactions spin more efficiently in oil and water than in gas, the relaxation time for oil is shorter than that of gas. For lighter components, the intermolecular and intramolecular dipole relaxation processes are related to the chain length. Bitumen has a short T_2 relaxation time, with T_1/T_2 ratios ranging from 100 to 1000 or higher as the asphaltene viscosity increases. For heavier components, the presence of asphaltenes and their aggregated states leads to interactions between protons and asphaltenes and between protons and paramagnetic ions and free radicals in asphaltenes. The interactions reduce relaxation times for T_1/T_2 ratios of ~10–1000 at the setting temperature (313 K). The general region of the components in this study can be divided into four regions using the T_2 distribution of the saturated core sample in Fig. 2. Region 1 represents the oil in cracks, where the dipole interaction spin and T_1–T_2 relaxation are close to those of the bulk fluids. The fluid in Region 1 had relatively long T_1 and T_2 relaxation times, and the T_1/T_2 ratio was close to 1. Region 2 represents the oil in macropores, with an average T_2 of 50 ms and a T_1/T_2 ratio ranging from 2 to 100. Regions 3 and 4 represent the oil in the micropores. Both T_1 and T_2 relaxation times in Region 3 were very short, denoting the low viscosity of the oil. Region 4 had a large T_1/T_2 ratio with a very short T_2 relaxation time, which most likely indicated oil with higher bituminous viscosity. The increase in the average chain length or viscosity of the remaining components led to shorter T_2 relaxation that were reflected in the leftward migration of the spectrum on the T_1–T_2 map and might have caused the overlap between Regions 2 and 4 in Fig. 8.

Figs. 9 and 10 show the T_1–T_2 spectrum maps for immiscible and miscible displacements of the core samples for different fractional

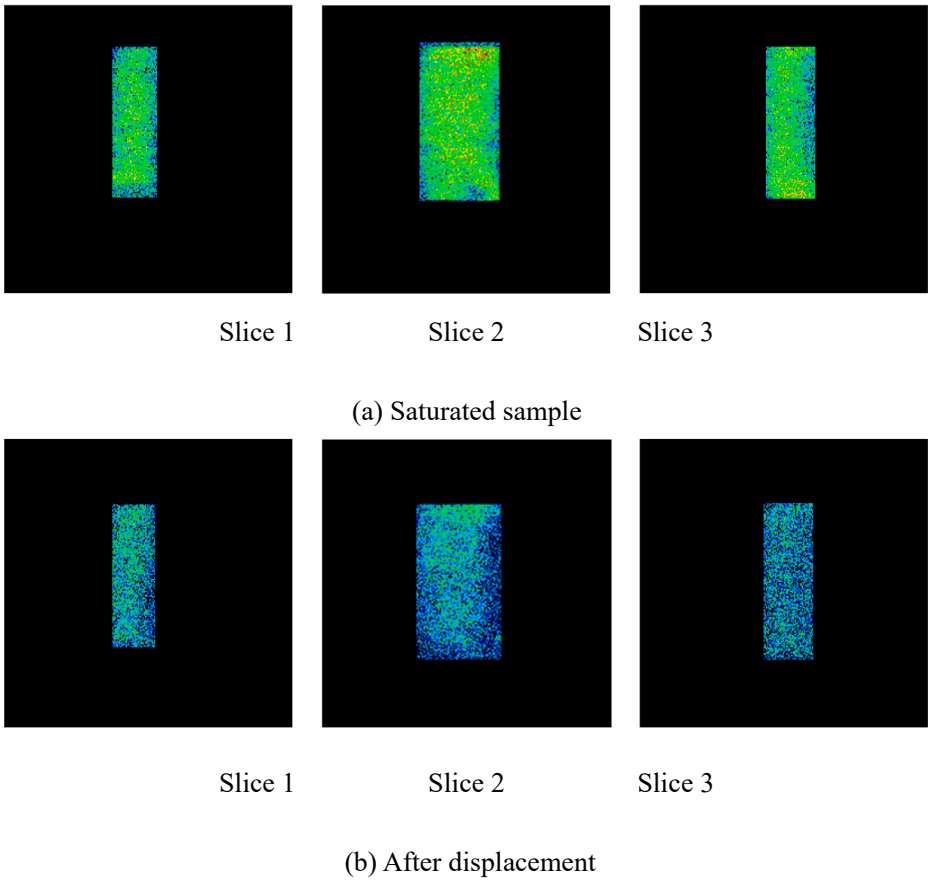

Fig. 6. MRI of oil saturation pre-and post-miscible flooding.

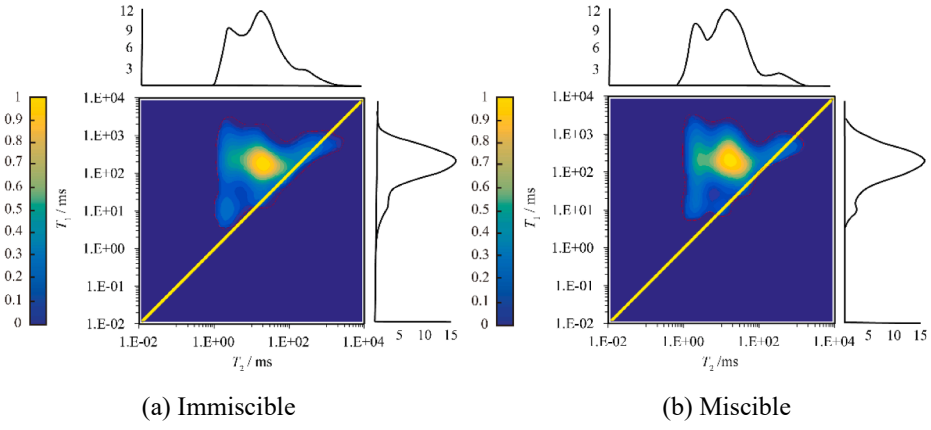

Fig. 7. T_1-T_2 spectra of saturated cores before immiscible (a) or miscible (b) displacement.

injections of CO_2. For immiscible flooding, oil expansion decreases the viscosity and was reflected in a T_1/T_2 ratio approaching 1 in Region 2 after a CO_2 injection of 0.2 PV (Fig. 9(b)). Subsequently, the extraction of light components by CO_2 resulted in a higher proportion of heavier components in the remaining oil and significantly decreased signal in Region 3 after a CO_2 injection of 0.4 PV (Fig. 9(c)). Long T_1 and T_2 relaxation times toward the far right of Region 1 are almost absent because oil was driven from the cracks (Fig. 9(d)).

Oil in cracks and macropores was displaced more efficiently by miscible flooding than by immiscible displacement, leading to the disappearance of the signal in Region 1 and in the right portion of Region 2 (Fig. 10(c)). The response in Region 3 was more robust, whereas the signal in Region 4 was correspondingly weak (Fig. 10(d)) due to the decreased oil viscosity in the micropores after CO_2 diffusion into the oil. The effect of the lighter component extraction on the oil viscosity and displacement efficiency was negligible in the miscible process.

3.3. *Displacement front evolution*

The transition zone between the displacing agent and the oil, which is perpendicular to the flow direction was defined as the displacement front. The results of the lattice Boltzmann simulation reflect multiphase flow at the pore scale, and the width of the displacement front is related to the miscibility between the two fluids and the complexity of the

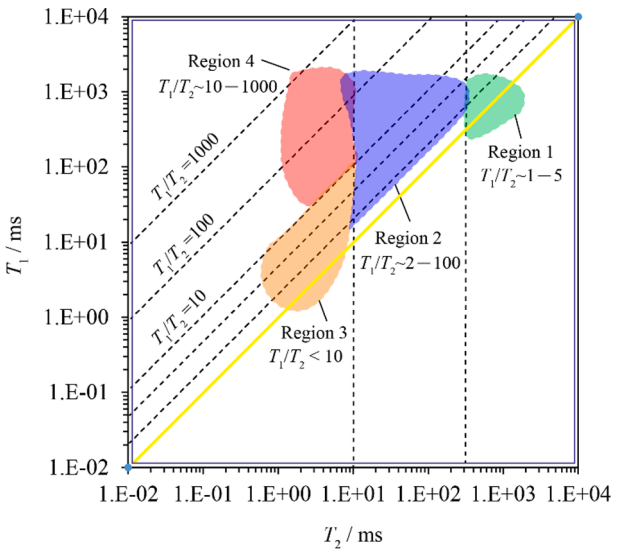

Fig. 8. General positions of different regions in the T_1-vs-T_2 map (modified after Li et al. [49], Fleury et al. [50], and Khatibi et al. [48]).

porous media structure [51]. At the core scale, the displacement front can be classified into three categories based on the miscibility of the two fluids. For two completely immiscible fluids, the mutual solubility can be ignored (e.g., for CO_2 and water), and there is an apparent interface between them [51]. Fig. 11(a) shows that Region I represents bulk fluids, including CO_2 and water shaded in blue and red, respectively; whereas Region II (in green) represents the narrow interface region. However, when CO_2 is used as a displacing agent to replace oil in a porous medium, the high solubility of CO_2 in the hydrocarbon creates a CO_2-oil transition zone (Fig. 11(b)). Interfacial tension remains a significant force throughout the region, leading relatively high residual oil saturation—especially in smaller pores and throats, where a larger pressure difference is required to overcome the capillary pressure. Thus, the transition zone in immiscible flooding is defined as an interfacial region of finite width across which most of the concentration change occurs and in which a surface tension force is accommodated [52]. In the initial state before CO_2 diffusion into the oil, the CO_2 concentration in the system is indicated by the red dotted line *a* in Fig. 11(b). At the static equilibrium of CO_2 and oil, the CO_2 concentration distribution is indicated by the red dotted line *b* after CO_2 dissolved into the oil. Consequently, the CO_2 concentration in the dynamic displacement process is shown as a solid black line between *a* and *b*, which is consistent with the theory.

This transition zone is analogously observed during miscible flooding as the concentration of CO_2 asymptotically approaches solubility in the bulk oil phase (Fig. 11(c)). The remaining oil is in contact with the continuously injected CO_2, and interfacial tension is present until complete miscibility is achieved. Therefore, when static equilibrium is reached, CO_2 is evenly distributed throughout the region, as indicated by the red dotted line *b*. When the system reaches the MMP condition, distinguishing between the dissolution and miscibility of CO_2 is meaningless. However, because the miscible process requires continuous forward or backward contact with CO_2, the concentration gradient at the miscible front should theoretically be higher than that at the transition front in the immiscible state. In this study, we defined the miscible front as the value corresponding to the intersection point M of the CO_2 concentration distribution curve in the dynamic and initial states (Fig. 11(c)). In the region downstream of M, CO_2 promotes oil recovery by dissolving and expanding the oil; whereas in the region upstream of M,

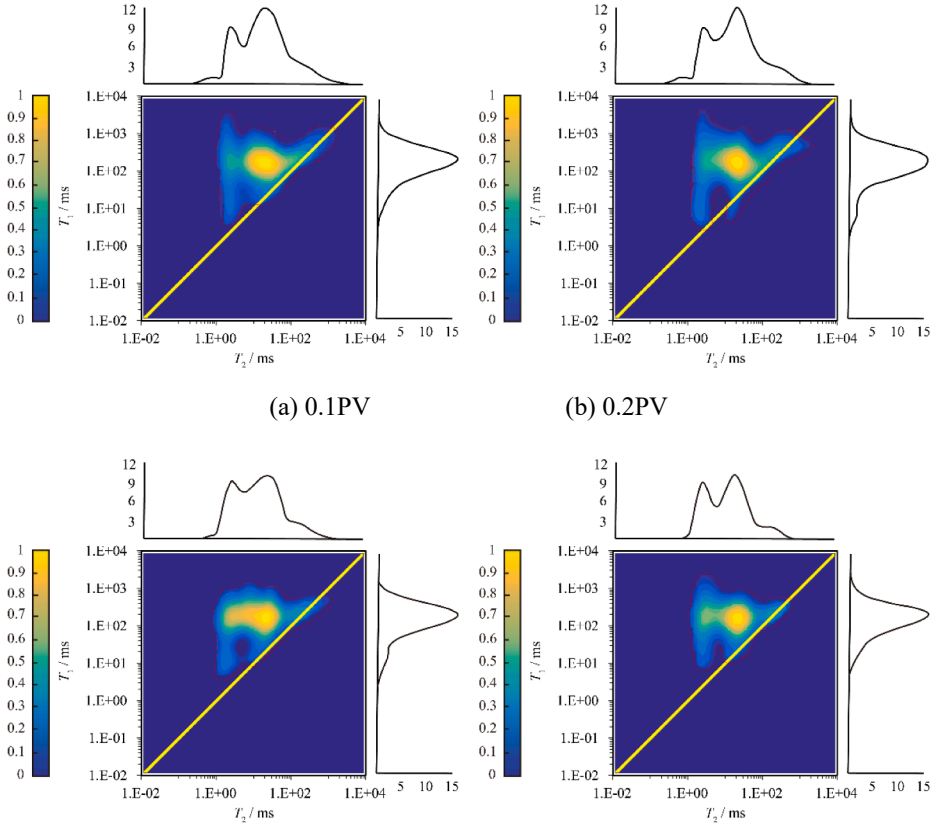

Fig. 9. Changes in the T_1-T_2 spectrum map with CO_2 injected in immiscible displacement.

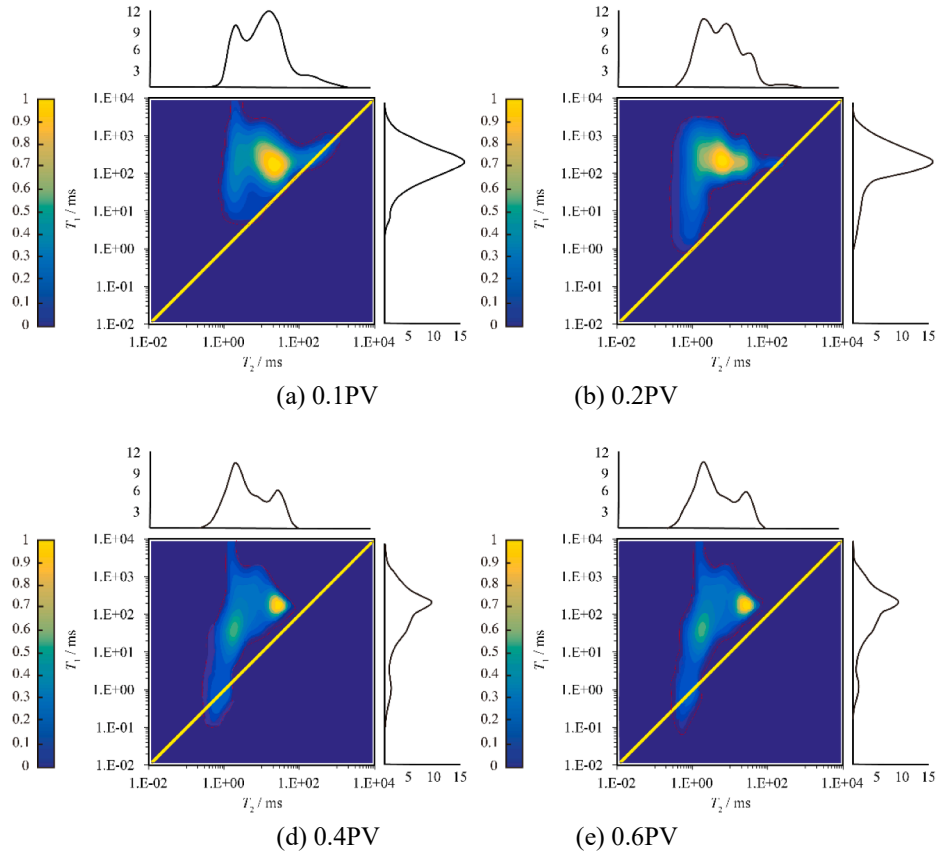

Fig. 10. Changes in the T_1-T_2 spectrum map with CO_2 injected in miscible displacement.

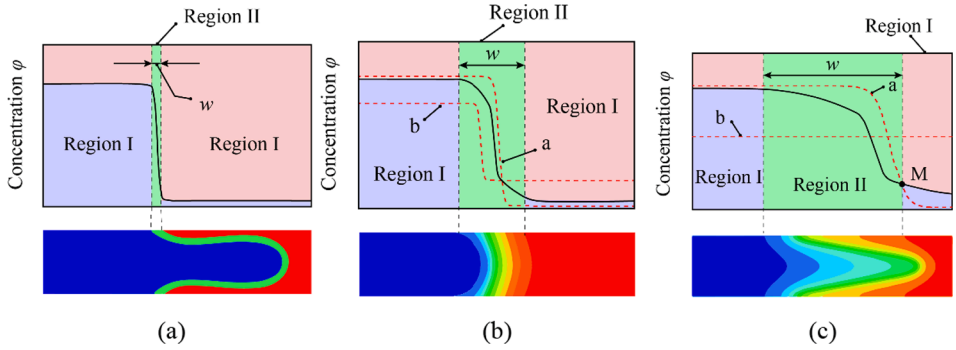

Fig. 11. Interfacial region and CO_2 concentration distributions of immiscible (a), partially dissolved (b), and miscible (c) fluids.

the interfacial tension decreases rapidly, and the oil is driven out of the smaller pores.

Fig. 12 shows the region of interest (ROI) and the location of Region II in the NMR displacement experiment. CO_2 was introduced at A, and

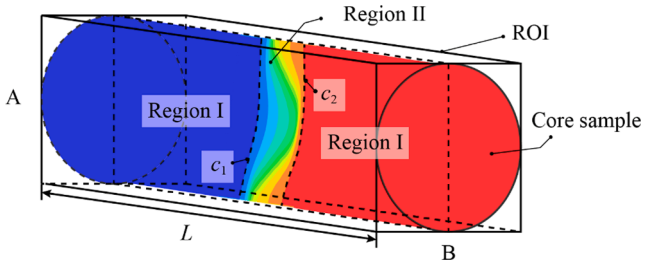

Fig. 12. Schematic of ROI and core sample.

CO_2 + oil was discharged at B. Contour c_1 represents the CO_2 displacement front (referred to as the CO_2 front), and c_2 represents the transition zone (immiscible state) or the front of the miscible zone (miscible state) in the displacement processes. According to the observed change in oil recovery during miscible/immiscible flooding (Fig. 3), the production rate slowed with immiscible and miscible flooding displacements of 0.6 and 0.4 PV, respectively. The CO_2 front c_1 is thought to migrate to the ROI outlet (B) at this stage. Therefore, the overall CO_2 front amplitude reductions for immiscible and miscible flooding were ~28% and 57%, respectively. Moreover, the description in Fig. 11(c) indicates the inclusion of a miscible zone within the transition zone when the miscible condition is achieved; the miscible front is considered to have a similar concentration to the CO_2 front in the immiscible state, with an ~ 28% amplitude reduction.

We define a dimensionless location as $X = x/L$, where x represents the distance downstream, and L is the total length of the ROV. Fig. 13

shows the CO_2 concentration (mole fraction) in the dimensionless coordinate system; the black curve represents the changing CO_2 concentration, and the shaded area T_{CO_2} denotes the average CO_2 concentration (mole fraction) within the entire ROI. α_2 is the equilibrium solubility of CO_2 in the predominantly oil-phase, with $1-\alpha_1$ the equilibrium solubility of oil in the predominantly-CO_2 phase. Thus, the dimensionless transition zone width at time i can be evaluated as:

$$w_i = \frac{T_{CO_2,i} - c_{1,i}\left(h_i(c_{1,i})\alpha_1 - \alpha_2\right) - \alpha_2}{C\left(h_i(c_{1,i})\alpha_1 - \alpha_2\right)} \tag{5}$$

$$h_i(c_{1,i}) = 1 - G_i(c_{1,i})\overline{c}_{1,i} \tag{6}$$

where $h(c_1)$ is a correction to accommodate viscous fingering of CO_2 in the core sample, $G(c_1)$ is the slope of the oil concentration between the inlet at A and position c_1,$\overline{c}_{1,i}$ is a dimensional position (mm), C is a constant related to the CO_2 concentration in the transition zone, and i represents the gas injection time. As gas is injected at a fixed rate in the experiment, i can also be expressed by the injected volume.

Owing to the low CO_2 concentration in the transition zone front, we assumed the absence of vapor-phase CO_2. Therefore, the amplitude reduction in the transition zone front is representative of the CO_2 concentration in the oil phase. To obtain the remaining mole fraction of CO_2 in the core, the molar volume of CO_2, the molar volume of oil, and the K-value of CO_2 should be determined by flash calculation. The molar volumes of CO_2 and oil samples under immiscibility conditions (8 MPa, 313 K) are 154.56 and 342.33 mL/mol, respectively. Moreover, when the molar fraction of CO_2 is 30%–98% in the collection reservoir (0.101 MPa, 299.2 K), the equilibrium constant of CO_2 in oil is ~51.96–50.18; the change in hydrocarbon components caused by the production was ignored. Table 3 shows the calculation results of the produced CO_2, the residual oil, and the CO_2 molar fraction in the core at each stage of immiscible flooding. According to the proposed T_1-T_2 map in Section 3.2, the extraction effect of CO_2 on lighter components in micropores was also analyzed; Fig. 16 shows the results. After immiscible CO_2 injection of 0.6 PV, the proportion of residual lighter components ($C_{1\sim6}$) decreased to 55% of the initial composition (18%). Coefficients α_1 and α_2 are defined as 1 and 0.1, respectively, based on the lattice Boltzmann simulation results of CO_2 flooding in porous media conducted by Aursjø et al. [52]. C is 0.5, and c_1 is 0.125 and determined by the 28% amplitude reduction (marked by the red line) on the 0.4 PV curve (Fig. 14). The CO_2 front (with an amplitude reduction of ~28%) appears for the first time in the ROI after a gas injection of 0.4 PV. The corresponding T_{CO_2} was 52% (Table 3). $G_{0.4PV}(0.125)$ was calculated at 0.091. The width of the transition zone $w_{0.4PV}$ is obtained by substituting the parameters into Eqs. (3) and (4), respectively:

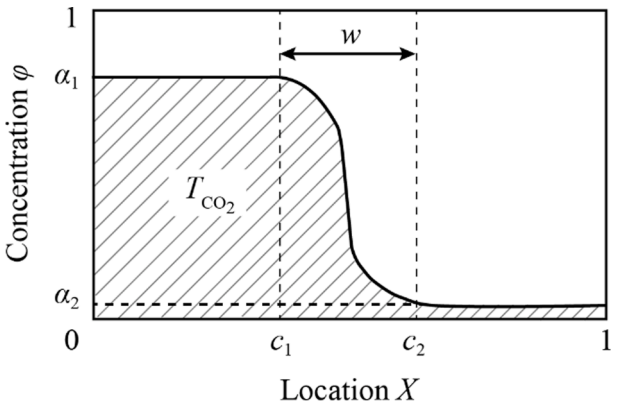

Fig. 13. CO_2 concentration profile in the dimensionless coordinate system, X.

Table 3
Experimental and computational results for immiscible flooding.

Injection Volume /PV	Cumulative gas injection/ mol	Cumulative gas production/ mol	Residual oil /mol	CO_2 mole fraction (T_{CO_2})	Reduction in amplitude
0.1	3.28×10^{-3}	0	1.35×10^{-2}	20%	9%
0.2	6.56×10^{-3}	0	1.26×10^{-2}	34%	15%
0.4	1.31×10^{-2}	0	1.20×10^{-2}	52%	19%
0.6	1.97×10^{-2}	1.23×10^{-4}	1.07×10^{-2}	65%	28%
0.8	2.62×10^{-2}	4.58×10^{-4}	1.03×10^{-2}	72%	31%
1.0	3.28×10^{-2}	1.32×10^{-3}	1.01×10^{-2}	76%	32%
1.2	3.94×10^{-2}	3.23×10^{-3}	1.00×10^{-2}	78%	32%
1.5	4.92×10^{-2}	7.12×10^{-3}	9.98×10^{-3}	81%	33%

$$w_{0.4PV} = \frac{T_{CO_2,0.4PV} - c_{1,0.4PV}\left[\left(1 - G_{0.4PV}\left(c_{1,0.4PV}\right)c_{1,0.4PV}\right)\alpha_1 - \alpha_2\right] - \alpha_2}{C\left[\left(1 - G_{0.4PV}(c_{1,0.4PV})c_{1,0.4PV}\right)\alpha_1 - \alpha_2\right]}$$
$$= 0.760$$

$w_{0.4PV}$ is the dimensionless width of the transition zone after 0.4 PV of gas injection, and c_2 is calculated as 0.885. This method estimates the width of the transition zone that appears in the ROI according to the 1D-FQ spatial distribution of the NMR amplitude.

For miscible flooding, a miscible zone is defined as range smaller than the transition zone. Because the concentration of the miscible front can be determined by the concentration of the CO_2 front during the immiscible flooding of the same oil sample, the width of the miscible zone ($w^{'}$) is directly determined by the 1D-FQ distribution (Fig. 15). $c_1^{'}$ is ~ 0, and $c_2^{'}$ is 0.44; thus, the width of the miscible zone $w^{'}$ is determined to be 0.44.

Under miscible conditions (16 MPa, 313 K), the molar volumes of CO_2 and oil are 57.33 and 340.80 mL/mol, respectively. Table 4 shows the calculated results for the produced CO_2, residual oil, and CO_2 molar fraction in the core at each stage of miscible flooding. The proportion of residual lighter components ($C_{1\sim6}$) in the micropores (black line, Fig. 16) inconspicuously declined from 18% to ~a17%. The CO_2 concentration of the miscible front α_2 can be derived from Eq. (5) as:

$$\alpha_2^{'} = \frac{T_{CO_2,i} - CCw_i^{'}h_i(c_{1,i})\alpha_1^{'}}{1 - c_{1,i}^{'} - Cw_i^{'}} = 0.526 \tag{7}$$

3.4. CO_2 trapping mechanisms

Another issue of concern for CO_2-EOR is the trapping of injected CO_2 in the porous medium [53–56]. The overall retention rate of CO_2 can be calculated from the cumulative mass of injected gas relative to the mass of gas measured at the outlet as follows:

$$R_{CO_2} = \frac{M_{ret}}{M_{in}} \times 100\% = \frac{M_{in} - M_{out} - M_{out}/K_{CO_2}}{M_{in}} \times 100\% \tag{8}$$

where M_{ret} is the number of moles of retained gas; M_{in} and M_{out} are the number of moles of injected and produced gas, respectively; and K_{CO_2} is the equilibrium constant of CO_2 in oil at 0.101 MPa and 299.2 K. Fig. 16 shows the miscible and immiscible flooding results. At the end of the displacement, the CO_2 retention rate for immiscible flooding of 85.24% was 10.59% lower than that for miscible flooding. Owing to the limited injection time and neglecting the effects of pressure drop and gas leakage, the experimental results likely overestimated the CO_2 retention

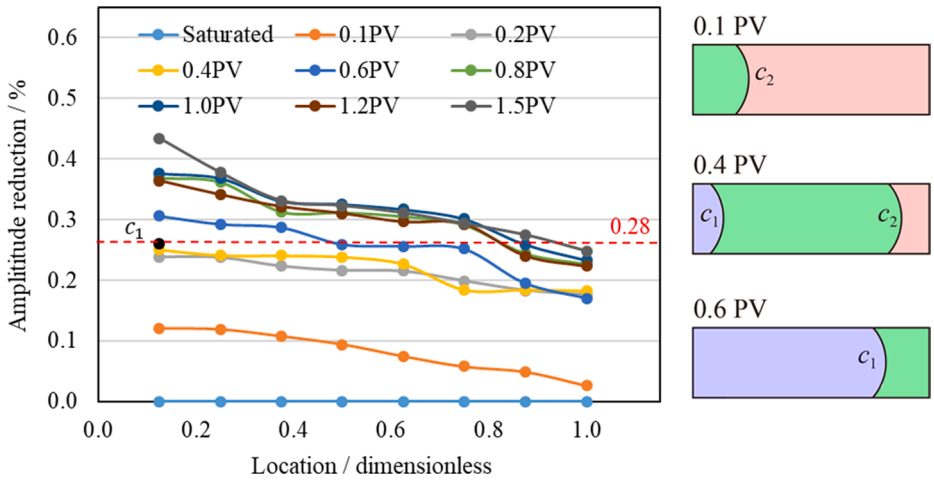

Fig. 14. Distribution of amplitude reduction for different gas injection volumes for immiscible flooding.

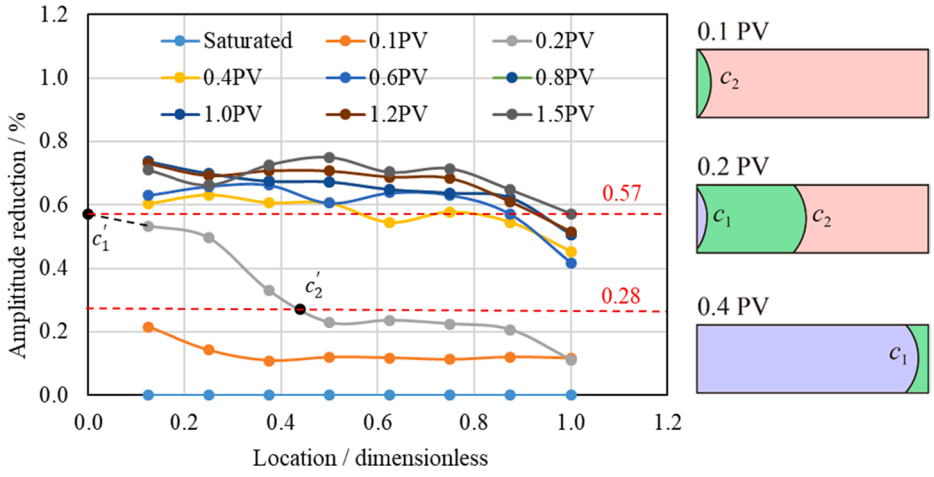

Fig. 15. Distribution of amplitude reduction for different gas injection volumes for miscible flooding.

Table 4
Experimental and computational results for miscible flooding.

Injection Volume /PV	Cumulative gas injection/ mol	Cumulative gas production/ mol	Residual oil / mol	CO_2 mole fraction (T_{CO_2})	Reduction in amplitude
0.1	9.04×10^{-3}	0	1.33×10^{-2}	40%	13%
0.2	1.81×10^{-2}	0	1.06×10^{-2}	63%	30%
0.4	3.62×10^{-2}	2.05×10^{-5}	6.48×10^{-3}	85%	57%
0.6	5.43×10^{-2}	2.87×10^{-4}	5.83×10^{-3}	90%	62%
0.8	7.23×10^{-2}	8.51×10^{-4}	5.17×10^{-3}	93%	66%
1.0	9.04×10^{-2}	1.81×10^{-3}	4.83×10^{-3}	95%	68%
1.2	1.09×10^{-1}	4.09×10^{-3}	4.76×10^{-3}	96%	69%
1.5	1.36×10^{-1}	8.49×10^{-3}	4.65×10^{-3}	96%	69%

rate but reflected the relative masses retained under miscible and immiscible conditions, respectively. As the injection volume increases and the reservoir pressure decreases, the CO_2 retention rate in the formation continues decreasing by ~10%–12%, as shown in some simulations [57,58].

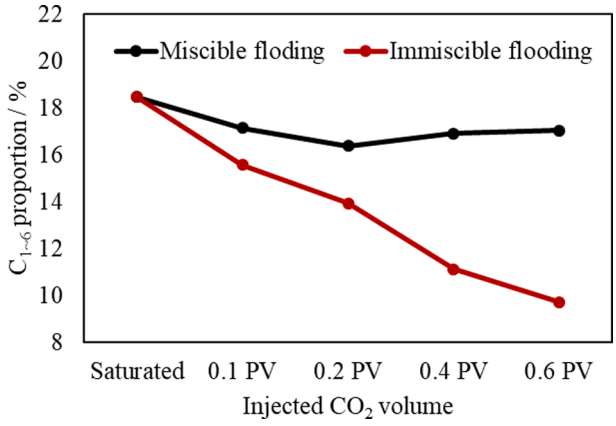

Fig. 16. Changes in $C_{1\sim6}$ proportion in micropores with CO_2 injection.

When the system pressure is higher than the MMP, CO_2 and oil mix intensively, elimination gas saturation in the core plug. Thus, the remaining oil fills the entire pore space in the liquid phase, and the swelling factor can be calculated directly as:

$$SF_{mis} = SF_{max} = \frac{V_p}{V_{ro}} = \frac{1}{A_{ro}} \tag{9}$$

where SF_{mis} is the swelling factor in the miscible state, SF_{max} is the maximum swelling factor when CO_2 is only in the liquid phase, V_p is the pore volume, V_{ro} is the pre-expansion equivalent volume of residual oil, and A_{ro} is the residual T_2 amplitude of oil.

However, for immiscible flooding, CO_2 cannot completely dissolve in oil when the CO_2 mole fraction exceeds the threshold. Fig. 17 shows a saturation pressure series with the injected CO_2 of the oil and CO_2 (initial composition) mixtures. The black line indicates an initial CO_2 concentration in the system of 10%. The saturation pressure increases as the initial concentration increases through CO_2 injection. The current phases of the mixtures with different compositions are demarcated as the immiscible flooding condition (8 MPa) with the dotted line. The region below the dotted line represents the entire liquid system, whereas the region above the line may contain both vapor and liquid phases. Thus, gas saturation may exist in the cores under immiscible flooding, depending on the initial composition and amount of injected CO_2. However, there is no vapor phase if CO_2 and the initial mixtures are completely miscible at 16 MPa.

Fig. 18 shows the oil swelling factor, which is used to describe the oil expansion under saturation pressure. Similarly, the swelling factor increases as the initial and injected CO_2 increase. A continuous injection of 70% CO_2 would cause the volume of the mixture to swell to nearly twice the original volume. Thus, when pre-existing CO_2 within a porous medium has full access to the oil, the subsequent injection of CO_2 may result in a more significant volume expansion. In this sense, a low injection rate and CO_2 soaking before production could enhance oil recovery.

Consequently, quantitatively characterizing the magnitudes of solubility trapping and residual trapping is necessary. We assumed that the injected CO_2 could completely dissolve in the oil phase before the gas was collected at the outlet, and that the relevant parameters should simultaneously satisfy the following conditions. First, the swelling factor for immiscible flooding is always smaller than the maximum swelling factor when CO_2 is fully dissolved ($SF_{im} < SF_{max}$). Second, the swelling factor at time i is larger than that at time $i-1$ ($SF_{im}(i) > SF_{im}(i-1)$). Third, the volume of vapor-phase CO_2 at time i is greater than that at time $i-1$ and smaller than the volume when oil expansion is ignored ($V_{CO_2}(i-1) < V_{CO_2}(i) < V_{CO_2}\_max$). Then, the minimum swelling factor SF_{min} can be calculated by successive resubstitution (exhaustive enumeration), and the swelling factor of immiscible flooding satisfy$SF_{min} < SF_{im} < SF_{max}$. Table 5 lists the results.

Point P in Fig. 19 (a) indicates the appearance of the vapor phase in the core; the upper and lower dashed lines represent the maximum and minimum swelling factors of oil, respectively. Thus, the actual swelling factors (SF_{im}) were located in the shaded area between these limits. Fig. 19(b) shows the change in the oil swelling factor (SF_{mis}) during miscible flooding. SF_{mis} can be more than double that of SF_{im} at the same

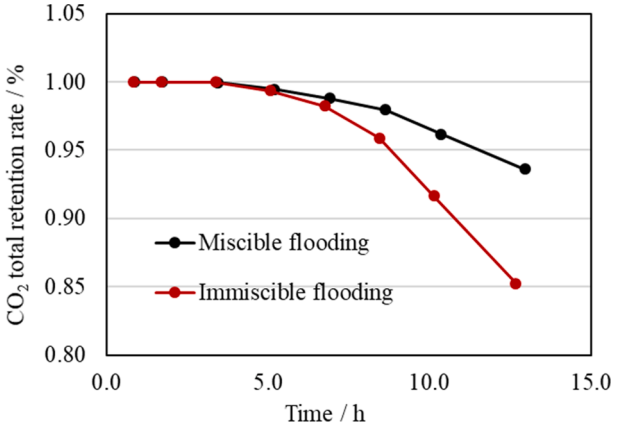

Fig. 17. Changes in CO_2 retention rate with time.

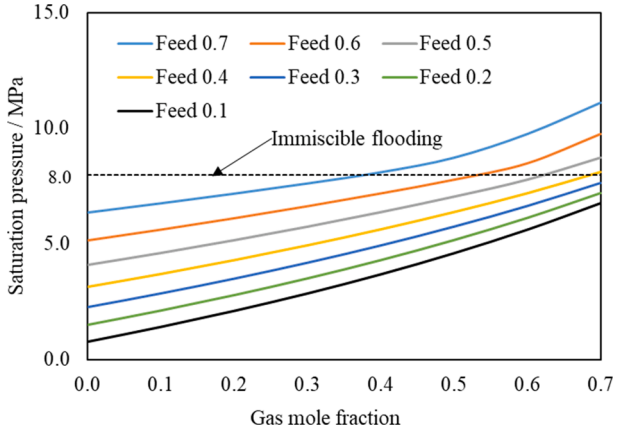

Fig. 18. Changes in saturation pressure with gas injection by respective mole fraction.

injection time; however, the amount of CO_2 used for miscible flooding (Table 4) is ~2.76 times that for immiscible flooding (Table 3) because of the higher pressure condition. This phenomenon indicates that oil expansion is more sensitive to the mass of injected CO_2 than to the original reservoir pressure.

Fig. 20 shows the switch between the trapping mechanisms. The blue and green areas represent the changes in CO_2 solubility trapping and residual trapping with injection time, respectively. The red line represents the maximum residual trapping rate. The data in Fig. 20 necessarily overestimate the amount of residual trapping but nonetheless represent the trend in the relative trapped contents by different methods. Fig. 21 is drawn according to the calculation results shown in Fig. 17 (total CO_2 retention in immiscible flooding) and Fig. 20(a) (oil volume expansion in immiscible flooding).

Residual trapping begins after the initiation of displacement; however, solubility trapping begins immediately. The residual trapping ratio rises sharply after the vapor phase separates, peaks at ~18%, and subsequently falls slowly. The slight decrease in the residual trapping ratio may be related to the diffusion rate of CO_2 in the porous medium and in the oil, which is affected by the difference in the CO_2 concentration between the oil interface, the complexity of pore-throat connectivity, and the CO_2-oil viscosity difference. As displacement progresses, residual oil may no longer be displaced under immiscible flooding conditions; thus, the residual trapping ratio approaches a fixed value limited to 12.89%. The injection pump is turned off for NMR scanning (to obtain data, including the T_2 spectrum, one-dimensional multilayer imaging, and the T_1–T_2 spectrum) at each measuring point and turned on again to inject CO_2. Therefore, the entire process is more like CO_2 injection–soaking–injection rather than continuous CO_2 injection. CO_2 has sufficient time to come into contact with oil in the porous media, allowing sufficient concentration diffusion. This may be the reason why the solubility trapping in this work is higher than the actual continuous CO_2 flooding at the field scale.

4. Conclusions

We developed a new methodology combining online NMR observation and analysis constrained by the T_1/T_2 ratio, one-dimensional frequency (1D-FQ), and magnetic resonance imaging (MRI) to overcome current experimental limitations for quantifying CO_2 diffusion and miscibility, oil swelling, light-component extraction, and CO_2 trapping in low-permeability porous media. The detailed outcomes are as follows:

1) NMR and MRI observations were synthesized, and oil PMR signals classifying separate pore size populations (including micropores, macropores, and cracks) were analyzed. CO_2 miscibility promoted the gradual replacement of oil in micropores, resulting in a final

Table 5
Swelling factor and CO_2 trapping for immiscible and miscible flooding.

Injection Volume/PV	Immiscible flooding				Miscible flooding	
	SF_{max}	SF_{min}	Maximum residual trapping /10^{-2}mol	Minimum solubility trapping /10^{-2}mol	SF_{mis}	Solubility trapping /10^{-2}mol
0.1	1.0971	1.0971	0	0.3281	1.1431	0
0.2	1.1756	1.1756	0	0.6562	1.4305	0.3281
0.4	1.2393	1.2393	0	1.3124	2.3471	0.6562
0.6	1.3820	1.2394	0.3386	1.6175	2.6111	1.3124
0.8	1.4447	1.2395	0.4660	2.1120	2.9420	1.6175
1.0	1.4614	1.2396	0.4979	2.6483	3.1475	2.1120
1.2	1.4757	1.2397	0.5248	3.0835	3.1975	2.6483
1.5	1.4846	1.2398	0.5409	3.6541	3.2686	3.0835

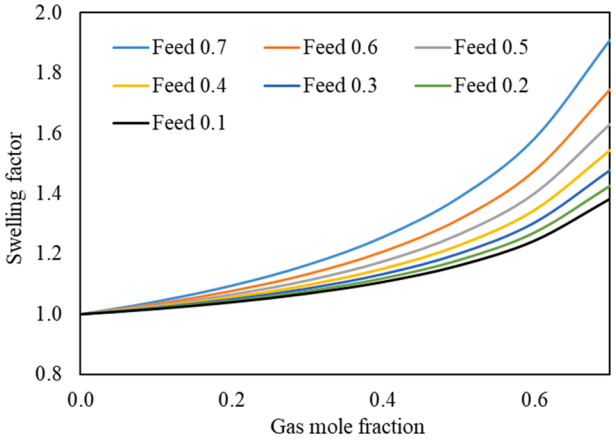

Fig. 19. Changes in swelling factor with gas injection by respective mole fraction.

recovery almost double that yielded by immiscible flooding alone (32.6%).

2) We further refined the demarcation of regions on the T_1–T_2 pattern map for oil-bearing tight (low-permeability) sandstones into four characteristic regions to describe the correlations between the NMR T_1/T_2 ratio and oil/gas mobility in porous media. The comparison shows that the extraction of lighter components remains negligible in miscible flooding and has little impact on the analysis, but increases the density in immiscible flooding.
3) The evolutions of CO_2-oil interfacial regions in immiscible and miscible flooding were analyzed to clarify the concepts of this transition and the development of a miscible zone/band. Correspondingly, a calculation method defining the CO_2-oil transition and miscible zone widths and front concentrations based on the 1D-FQ spatial distribution was proposed. The transition zone analysis for the immiscible state is the premise for studying the miscible zone of the same sample.
4) An analytical method combining the mass balance of the influent (CO_2) and effluent fluids (CO_2 and oil) and the vapor–liquid equilibrium was proposed to reveal the relative contributions of solubility and residual trapping. The residual trapping ratio after immiscible flooding in this work did not exceed 12.9%, with a total CO_2 retention rate 10.6% lower than that of miscible flooding.

CRediT authorship contribution statement

Mingyu Cai: Data curation, Methodology, Writing – original draft. **Yuliang Su:** Supervision. **Yongmao Hao:** Methodology. **Yingchun Guo:** Methodology. **Derek Elsworth:** Writing - review & editing. **Lei Li:** Investigation. **Dongsheng Li:** Investigation. **Xinyu Li:** Investigation.

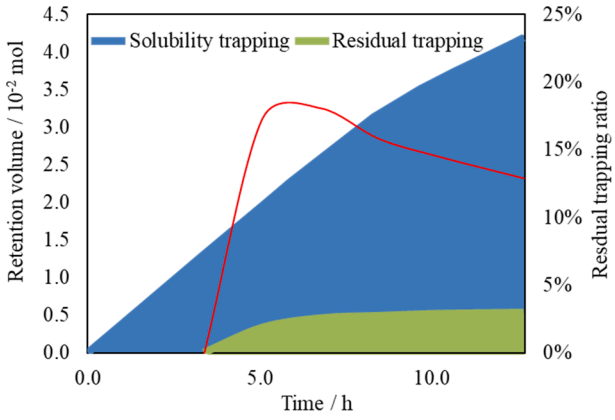

Fig. 21. Change in CO_2 trapping mode in immiscible flooding.

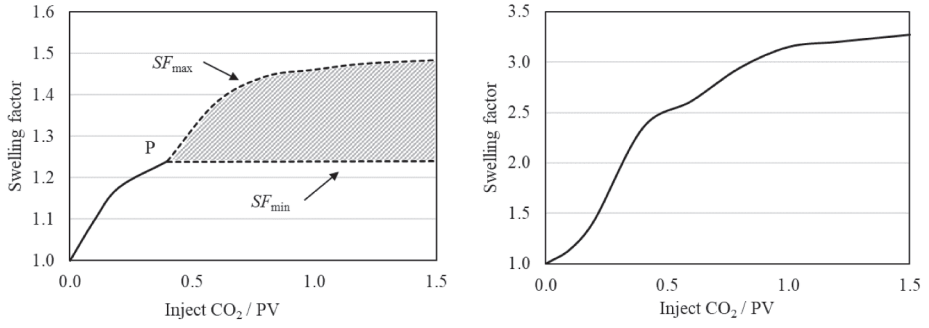

(a) Immiscible flooding (b) Miscible flooding

Fig. 20. Changes in swelling factor with CO_2 volume for immiscible (a) and miscible (b) flooding.

Declaration of Competing Interest

The authors declare that they have no known competing financial interests or personal relationships that could have appeared to influence the work reported in this paper.

Acknowledgments

This project was supported by the National Natural Science Foundation of China (No. 51974348, 51904324), the Science and Technology Planning Project of Guizhou Province (No. Qian Ke He [2020]2Y028th), the Graduate Innovative Engineering Project of China University of Petroleum (No. YCX2018017).

References

[1] Zhang Y, Gao M, You Q, Fan H, Li W, Liu Y, et al. Smart mobility control agent for enhanced oil recovery during CO2 flooding in ultra-low permeability reservoirs. Fuel 2019;241:442–50.
[2] Hoffman BT, Shoaib S. CO2 flooding to increase recovery for unconventional liquids-rich reservoirs. J Energy Res Technol 2014;136(2).
[3] Fang T, Zhang Y, Ding B, Yan Y, Zhang J. Static and dynamic behavior of CO2 enhanced oil recovery in nanoslits: Effects of mineral type and oil components. Int J Heat Mass Transf 2020;153:119583. https://doi.org/10.1016/j.ijheatmasstransfer.2020.119583.
[4] Ampomah W, Balch RS, Cather M, Will R, Gunda D, Dai Z, et al. Optimum design of CO2 storage and oil recovery under geological uncertainty. Appl Energy 2017;195:80–92.
[5] Zhang K, Jia Na, Li S, Liu L. Static and dynamic behavior of CO2 enhanced oil recovery in shale reservoirs: Experimental nanofluidics and theoretical models with dual-scale nanopores. Appl Energy 2019;255:113752. https://doi.org/10.1016/j.apenergy.2019.113752.
[6] Huang S, Cao M, Cheng L. Experimental study on the mechanism of enhanced oil recovery by multi-thermal fluid in offshore heavy oil. Int J Heat Mass Transf 2018;122:1074–84.
[7] Wang R, Peng F, Song K, Feng G, Guo Z. Molecular dynamics study of interfacial properties in CO2 enhanced oil recovery. Fluid Phase Equilib 2018;467:25–32.
[8] Torabi F, Qazvini Firouz A, Kavousi A, Asghari K. Comparative evaluation of immiscible, near miscible and miscible CO2 huff-n-puff to enhance oil recovery from a single matrix–fracture system (experimental and simulation studies). Fuel 2012;93:443–53.
[9] Othman F, Naufaliansyah MA, Hussain F. Effect of water salinity on permeability alteration during CO_2 sequestration. Adv Water Resour 2019;127:237–51.
[10] Zhou X, Yuan Q, Zhang Y, Wang H, Zeng F, Zhang L. Performance evaluation of CO2 flooding process in tight oil reservoir via experimental and numerical simulation studies. Fuel 2019;236:730–46.
[11] Sheng G, Su Y, Zhao H, Liu J. A unified apparent porosity/permeability model of organic porous media: Coupling complex pore structure and multi-migration mechanism. Adv Geo-Energy Res 2020;4(2):115–25.
[12] Zeng Q, Yao J, Shao J. An extended finite element solution for hydraulic fracturing with thermo-hydro-elastic–plastic coupling. Comput Methods Appl Mech Eng 2020;364:112967. https://doi.org/10.1016/j.cma.2020.112967.
[13] Li J, Wu K, Chen Z, Wang W, Yang B, Wang K, et al. Effects of energetic heterogeneity on gas adsorption and gas storage in geologic shale systems. Appl Energy 2019;251:113368.
[14] Cai M, Su Y, Elsworth D, Li L, Fan L. Hydro-mechanical-chemical modeling of sub-nanopore capillary-confinement on CO2-CCUS-EOR. Energy 2021;225:120203. https://doi.org/10.1016/j.energy.2021.120203.
[15] Zhan S, Su Y, Jin Z, Zhang M, Wang W, Hao Y, et al. Study of liquid-liquid two-phase flow in hydrophilic nanochannels by molecular simulations and theoretical modeling. Chem Eng J 2020;395:125053. https://doi.org/10.1016/j.cej.2020.125053.
[16] Dai Z, Middleton R, Viswanathan H, Fessenden-Rahn J, Bauman J, Pawar R, et al. An integrated framework for optimizing CO2 sequestration and enhanced oil recovery. Environ Sci Technol Lett 2014;1(1):49–54.
[17] Cai J, Zhang L, Wei W. Chapter 1 - A brief introduction to flow and transport in fractal porous media. In: Cai J, Zhang L, Wei W, editors. Modelling of Flow and Transport in Fractal Porous Media. Elsevier; 2021. p. 1–10.
[18] Sheng G, Su Y, Javadpour F, Wang W, Zhan S, Liu J, et al. New slip coefficient model considering adsorbed gas diffusion in shale gas reservoirs. Energy Fuels 2020;34(10):12078–87.
[19] Li J, Wu K, Chen Z, Wang K, Luo J, Xu J, et al. On the negative excess isotherms for methane adsorption at high pressure: modeling and experiment. SPE J 2019;24(06):2504-25.
[20] Bush I. NMR studies of enhanced oil recovery core floods and core analysis protocols. University of Cambridge; 2019.
[21] Wang D, Yao J, Chen Z, Song W, Sun H. Multiphase flow model from pores to cores in organic-rich shale. J Petrol Sci Eng 2020;194:107317. https://doi.org/10.1016/j.petrol.2020.107317.
[22] Song W, Yao J, Ma J, Sun H, Li Y, Yang Y, et al. Numerical simulation of multiphase flow in nanoporous organic matter with application to coal and gas shale systems. Water Resour Res 2018;54(2):1077–92.
[23] Liu L, Huang Z, Yao J, Di Y, Wu Y-S. An efficient hybrid model for 3D complex fractured vuggy reservoir simulation. SPE J 2020.
[24] Yesufu-Rufai S, Rücker M, Berg S, Lowe SF, Marcelis F, Georgiadis A, et al. Assessing the wetting state of minerals in complex sandstone rock in-situ by Atomic Force Microscopy (AFM). Fuel 2020;273:117807. https://doi.org/10.1016/j.fuel.2020.117807.
[25] Chandrasekhar S, Mohanty KK. Effect of brine composition on oil-rock interaction by atomic force microscopy. J Petrol Sci Eng 2018;164:289–301.
[26] Zimmerman U, Madland MV, Nermoen A, Hildebrand-Habel T, Bertolino SAR, Hiorth A, et al. Evaluation of the compositional changes during flooding of reactive fluids using scanning electron microscopy, nano-secondary ion mass spectrometry, x-ray diffraction, and whole-rock geochemistryCompositional Changes during Flooding. AAPG Bull 2015;99(05):791–805.
[27] Shi J-Q, Xue Z, Durucan S. Supercritical CO2 core flooding and imbibition in Tako sandstone—Influence of sub-core scale heterogeneity. Int J Greenhouse Gas Control 2011;5(1):75–87.
[28] Safari A, Dowlatabad MM, Hassani A, Rashidi F. Numerical simulation and X-ray imaging validation of wormhole propagation during acid core-flood experiments in a carbonate gas reservoir. J Nat Gas Sci Eng 2016;30:539–47.
[29] Zhao Y, Xue S, Han S, Chen Z, Liu S, Elsworth D, et al. Effects of microstructure on water imbibition in sandstones using X-ray computed tomography and neutron radiography. J Geophys Res Solid Earth 2017;122(7):4963–81.
[30] Sun X, Yao Y, Liu D, Elsworth D, Pan Z. Interactions and exchange of CO 2 and H 2 O in coals: an investigation by low-field NMR relaxation. Sci Rep 2016;6(1):1–11.
[31] Zheng S, Yao Y, Elsworth D, Liu D, Cai Y. Dynamic fluid interactions during CO2-ECBM and CO2 sequestration in coal seams. Part 2: CO2-H2O wettability. Fuel 2020;279:118560.
[32] Dong Xu, Shen LW, Liu X, Zhang P, Sun Y, Yan W, et al. NMR characterization of a tight sand's pore structures and fluid mobility: An experimental investigation for CO2 EOR potential. Mar Pet Geol 2020;118:104460. https://doi.org/10.1016/j.marpetgeo.2020.104460.
[33] Wei B, Zhang X, Wu R, Zou P, Gao K, Xu X, et al. Pore-scale monitoring of CO2 and N2 flooding processes in a tight formation under reservoir conditions using nuclear magnetic resonance (NMR): A case study. Fuel 2019;246:34–41.
[34] Dong Xu, Shen LW, Golsanami N, Liu X, Sun Y, Wang F, et al. How N2 injection improves the hydrocarbon recovery of CO2 HnP: An NMR study on the fluid displacement mechanisms. Fuel 2020;278:118286. https://doi.org/10.1016/j.fuel.2020.118286.
[35] Chizhik VI, Chernyshev YS, Donets AV, Frolov VV, Komolkin AV, Shelyapina MG, editors. Magnetic Resonance and Its Applications. Cham: Springer International Publishing; 2014.
[36] Li L, Han H, Balcom BJ. Spin echo SPI methods for quantitative analysis of fluids in porous media. J Magn Reson 2009;198(2):252–60.
[37] Hirasaki GJ, Lo S-W, Zhang Y. NMR properties of petroleum reservoir fluids. Magn Reson Imaging 2003;21(3-4):269–77.
[38] Sandor M, Cheng Y, Chen S. Improved correlations for heavy-oil viscosity prediction with NMR. J Petrol Sci Eng 2016;147:416–26.
[39] Ma Yu, Wang H, Wang W, Zhou S, Ding Y, Pan J, et al. The application of Nuclear Magnetic Resonance T1–T2 maps in the research of sedimentary organic matter: A case study of early mature shale with type I kerogen. J Petrol Sci Eng 2020;194:107447. https://doi.org/10.1016/j.petrol.2020.107447.
[40] Price WS. NMR Imaging. In: Webb GA, editor. Annual Reports on NMR Spectroscopy. Academic Press; 1998. p. 139–216.
[41] Chapter 5 NMR logging applications. In: Dunn KJ, Bergman DJ, Latorraca GA, editors. Handbook of Geophysical Exploration: Seismic Exploration. Pergamon; 2002, p. 129-64.
[42] Traficante DD. Can T2, be longer than T1? Concepts in Magnetic Resonance 1991;3(3):171–7.
[43] Korb J-P, Nicot B, Jolivet I. Dynamics and wettability of petroleum fluids in shale oil probed by 2D T1–T2 and fast field cycling NMR relaxation. Microporous Mesoporous Mater 2018;269:7–11.
[44] Anet FAL, O'Leary DJ. The shielding tensor. Part I: Understanding its symmetry properties. Concepts Magnet Resonance 1991;3(4):193–214.
[45] Jiang H, Daigle H, Tian X, Pyrcz MJ, Griffith C, Zhang B. A comparison of clustering algorithms applied to fluid characterization using NMR T1–T2 maps of shale. Comput Geosci 2019;126:52–61.
[46] Teng Y, Wang P, Jiang L, Liu Y, Song Y, Wei Y. An experimental study of density-driven convection of fluid pairs with viscosity contrast in porous media. Int J Heat Mass Transf 2020;152:119514. https://doi.org/10.1016/j.ijheatmasstransfer.2020.119514.
[47] Markovic S, Bryan JL, Turakhanov A, Cheremisin A, Mehta SA, Kantzas A. In-situ heavy oil viscosity prediction at high temperatures using low-field NMR relaxometry and nonlinear least squares. Fuel 2020;260:116328. https://doi.org/10.1016/j.fuel.2019.116328.
[48] Khatibi S, Ostadhassan M, Xie ZH, Gentzis T, Bubach B, Gan Z, et al. NMR relaxometry a new approach to detect geochemical properties of organic matter in tight shales. Fuel 2019;235:167–77.
[49] Li T, Huang Z, Feng Y, Chen X, Ma Q, Liu B, et al. Reservoir characteristics and evaluation of fluid mobility in organic-rich mixed siliciclastic-carbonate sediments: A case study of the lacustrine Qiketai Formation in Shengbei Sag, Turpan-Hami Basin, Northwest China. J Petrol Sci Eng 2020;185:106667. https://doi.org/10.1016/j.petrol.2019.106667.

[50] Fleury M, Romero-Sarmiento M. Characterization of shales using T1–T2 NMR maps. J Petrol Sci Eng 2016;137:55–62.
[51] Xu Z, Liu H, Valocchi AJ. Lattice B oltzmann simulation of immiscible two-phase flow with capillary valve effect in porous media. Water Resour Res 2017;53(5):3770–90.
[52] Aursjø O, Pride SR. Lattice Boltzmann method for diffusion-limited partial dissolution of fluids. Phys Rev E 2015;92(1):013306.
[53] Song Y-Q, Kausik R. NMR application in unconventional shale reservoirs–A new porous media research frontier. Prog Nucl Magn Reson Spectrosc 2019;112:17–33.
[54] Hussain R. NMR studies of carbon dioxide sequestration in porous media. University of Cambridge; 2015.
[55] Azzolina NA, Nakles DV, Gorecki CD, Peck WD, Ayash SC, Melzer LS, et al. CO2 storage associated with CO2 enhanced oil recovery: A statistical analysis of historical operations. Int J Greenhouse Gas Control 2015;37:384–97.
[56] Farajzadeh R, Eftekhari AA, Dafnomilis G, Lake LW, Bruining J. On the sustainability of CO2 storage through CO2–Enhanced oil recovery. Appl Energy 2020;261:114467. https://doi.org/10.1016/j.apenergy.2019.114467.
[57] Ren Bo, Duncan IJ. Reservoir simulation of carbon storage associated with CO2 EOR in residual oil zones, San Andres formation of West Texas, Permian Basin, USA. Energy 2019;167:391–401.
[58] Zhao X, Rui Z, Liao X. Case studies on the CO2 storage and EOR in heterogeneous, highly water-saturated, and extra-low permeability Chinese reservoirs. J Nat Gas Sci Eng 2016;29:275–83.